Robust LPV Fault Diagnosis Using the Set-Based Approach for Autonomous Ground Vehicles

Shuang Zhang, Vicenç Puig and Sara Ifqir

***Abstract*— This paper proposes a robust fault diagnosis method for Autonomous Ground Vehicles (AGVs) modeled as a Linear Parameter Varying (LPV) system with bounded uncertainties. The proposed approach combines the zonotope-based Set-Membership Approach (SMA) and Set Invariance Approach (SIA). Firstly, an online fault detection strategy based on zonotopic set-membership state estimation is introduced, where the optimal observer gain is calculated offline by solving LMI optimization problems. To characterize the Minimum Detectable Fault (MDF) and Minimum Isolable Fault (MIF), the invariant residual sets are first obtained for the system operated in healthy and faulty modes. The proposed method relies on the propagation of the zonotopic state estimation error in steady state based on SIA. Then, MDF and MIF are characterized for several types of faults by solving optimization problems subject to set separation conditions. Finally, experiment validations using a prototype vehicle are performed to illustrate the effectiveness of the proposed approach.**

***Index Terms*— Fault diagnosis, set invariance approach, set-membership approach, LPV, minimum detectable fault, minimum isolable fault, autonomous ground vehicles.**

I. Introduction

AUTONOMOUS Ground Vehicles (AGVs) have received considerable attention and are widely studied because of the significant advantages of reduction accidents, improving traffic efficiency, energy consumption, etc. To improve driving comfort and safety, in-vehicle Advanced Driver Assistance Systems, as e.g., parking assist and collision avoidance, have been developed a lot [1], [2]. To this end, AGVs are equipped with various actuators, sensors and control units [3], and become safety-critical systems. However, the actuators and sensors of AGVs can experience faults over time, i.e., the calibration drift of an IMU (Inertial Measurement Unit), the mechanical wear and tear on the mechanical components of the steering actuator, etc. Generally, faults of AGVs can be caused by various physical phenomena, such as actuator faults caused by freezing, loss of effectiveness or lock-in-place, and sensor faults resulting from bias or drift [4]. If these actuator and/or sensor faults are not handled in time, they may lead to catastrophic consequences. Therefore, detection and identification of faults are quite essential in order to be able to take corrective actions and ensure safety and reliability of the vehicle [5].

Hereby, great efforts have been devoted to the research on AGVs fault diagnosis. For instance, Rajamani et al. [6] proposed a fault diagnostic system for automated vehicles operating as a platoon. Luo et al. [7] developed an integrated model-based and data-driven fault diagnosis method for automotive antilock braking systems. Meskin and Khorasani [8] explored the problem of Fault Detection and Isolation (FDI) for a network of unmanned vehicles. Varrier et al. [9], [10] investigated the FDI problem for vehicle lateral dynamics. Arogeti et al. [11] developed an FDI framework using global analytical redundancy relations and applied it to an electrohydraulic vehicle steering system. Svärd et al. [12], [13] concentrated on the residual generation for fault detection of the engine. Pan et al. [14] detected the faults of both steering and torque actuators of AGVs using a nonlinear observer-based method. Existing fault diagnosis methods can be classified into data-based methods and model-based methods. These data-based fault diagnosis methods use hardware redundancy, limit confirmation, frequency spectrum analysis, among other to detect the occurred faults [15], which strongly depend on the quality of the collected data [14]. Different from the model-free methods, the model-based fault diagnosis methods rely on a mathematical model to describe the system behavior, which can be easily implemented onboard. In this regard, model-based fault diagnosis methods have been widely studied for AGVs [10], [13], [16], [17].

Among the tasks of fault diagnosis, Fault Detection and Isolation (FDI) algorithms play an important role in safety-critical systems due to their ability to detect and isolate failing components efficiently and rapidly. Model-based fault detection aims to check the consistency between the estimated behaviors using the mathematical model and the observations obtained from sensors by means of residuals. To achieve a satisfactory fault detection performance, the designed observer must be robust against unknown uncertainties (e.g., modeling uncertainty, unknown noise and disturbances) [13], [18]. One approach to model the uncertainties is based on the use of probabilistic methods, as proposed in [19]. However, this is not always possible unless the uncertainties are well modelled by stationary random processes with known

Manuscript received 5 August 2022; revised 31 May 2023 and 13 February 2024; accepted 8 April 2024. Date of publication 9 May 2024; date of current version 1 August 2024. This work was supported in part by Spanish State Research Agency (AEI), in part by European Regional Development Fund (ERFD) through the Project SaCoAV under Grant MINECO PID2020-114244RB-I00, and in part by Chinese Scholarship Council (CSC) under Grant 202006120006. The Associate Editor for this article was C. G. Panayiotou. *(Corresponding author: Vicenç Puig.)*

Shuang Zhang and Vicenç Puig are with the Institut de Robòtica i Informàtica Industrial, CSIC-UPC, 08028 Barcelona, Spain (e-mail: shuang.zhang@upc.edu; vicenc.puig@upc.edu).

Sara Ifqir is with CRIStAL, UMR CNRS 9189, Centrale Lille Institut, 59651 Villeneuve-d'Ascq, France (e-mail: sara.ifqir@centralelille.fr).

probabilistic distributions. An alternative way to achieve robust fault detection is by using set-based approaches such as Set-Membership Approach (SMA) and Set Invariance Approach (SIA), in which the uncertainties are assumed to be unknown but bounded by means of different type of sets, e.g. intervals [3], polytopes [20], ellipsoids [21] and zonotopes [22], [23]. SMA leads to detect the fault in both transient and steady-state operation of the system since its residual generation and evaluation are performed online [24]. On the other hand, SIA only works in steady-state since the residual characterization is performed offline. As the residual finally reaches an invariant set in each healthy or faulty operation mode of the system, fault detection can be performed as long as the healthy and faulty residual sets can be separated [25], [26]. Inspired by the above features of SMA and SIA, this paper aims to propose an FDI scheme combining an SMA-based online fault detection and an SIA-based offline fault characterisation of Minimum Detectable Fault (MDF) and Minimum Isolable Fault (MIF).

Furthermore, regarding the recent studies about set-based fault detection problems for AGVs, Ifqir et al. [3] developed an interval observer-based fault detection scheme for actuator/sensor fault of vehicle lateral dynamics. Reference [20] developed a polytope-based SIA to compute the MDF of the actuator/sensor fault of a practical vehicle. According to [24], zonotopes provide a much more compact representation than intervals, and more efficient computation compared with the huge number of vertices of the equivalent polytopes due to the simple matrix calculation. This motivates the proposed FDI scheme to be implemented using zonotope sets. Moreover, to the best of our knowledge, there is no literature on FDI using zonotope-based SMA and SIA for autonomous ground vehicles.

In order to conduct SIA-based FDI, it is vital to construct healthy and faulty invariant residual sets. There are several works on characterizing the residual invariant set with the well-established concepts of minimal Robust Positively Invariant (mRPI) sets [27], [28], [29] and Ultimate Bound Invariant (UBI) sets [30], [31] for Linear Time-Invariant (LTI) systems. However, as AGVs are complex systems and usually modelled as LPV systems, the methods of computing invariant sets for LPV systems are necessary. In [32] and [33], the authors developed ellipsoidal Robust Positively Invariant (RPI) sets by solving Linear Matrix Inequalities (LMIs) with a predefined common quadratic Lyapunov function, which is conservative to ensure the stability for all vertex systems of the LPV system. To reduce the conservatism, [20] employed a parameter-dependent Lyapunov function to guarantee the stability of the observer, and used a sequence of convex-set operations to compute mRPI sets.

Inspired by the aforementioned discussions, this paper proposed a robust LPV fault diagnosis scheme using a zonotope set-based approach for AGVs. First, a zonotope-based SMA with the optimal observer is proposed for the online fault detection, where the optimal observer gain is computed offline by solving an LMI optimization problem. Then, a zonotope-based SIA is employed to characterise the Minimum Detectable Fault (MDF) and Minimum Isolable Fault (MIF). Compared with the relevant existing literature [20], [22], [24], [34], the main contributions of this paper are:

- Different from the zonotopic observer proposed in [22], which employed the explicit solution of [35] to compute the optimal filter gain online, this paper generalises the design of a zonotopic observer to the set-membership case and calculates the optimal observer gain offline by solving an LMI optimization problem that minimizes the Frobenius norm. The offline solution facilitates real-time computations, which makes it a compelling choice for vehicle applications where computational resources are a critical issue.
- This paper provides a SIA-based approach to characterise MDF and MIF for the proposed SMA applied to vehicle lateral dynamic systems by using zonotopic RPI sets, which normally leads to a more precise MDF and MIF magnitude, compared with interval RPI sets proposed in [24].
- Different from the linear programming solution of the optimization problem in [20], the MDF computation problem in this paper is transformed into searching the intersection point by solving several equations, which provides a simpler solution. Moreover, this solution is successfully extended to the computation of MIF, which is not yet considered in the existing literature.
- The set separation theorem is extended to MIF computation for LPV systems. Note that the previous work [34] is only for MDF computation of LTI systems.

The structure of the paper is organized as follows: The problem formulation including a vehicle lateral dynamics model is presented in Section II. An on-line zonotopic set-membership based FDI is proposed in Section III. In Section IV, the construction of healthy and faulty zonotopic mRPI residual sets based on SIA and the computation of Minimun Detectable Fault (MDF) and Minimum Isolable Fault (MIF) through set separation are proposed. Experiment results using an autonomous ground vehicle are given in Section V to illustrate the effectiveness of the proposed approach. Finally, the conclusions are drawn in Section VI.

Notation: Throughout this paper, $\mathbb{R}^n$ denotes the set of n-dimensional real numbers and $\oplus$ denotes the Minkowski sum. The matrices are written using capital letter, e.g., A, the calligraphic notation is used for denoting sets, e.g., $\mathcal{X}$.

II. Problem Formulation

A. Vehicle Lateral Dynamics Model

Vehicle lateral dynamics may be modeled using a two degree of freedom model known as the "bicycle model" (see Figure 1) that describes the lateral and yaw motions [36]. The equations of this model are as follows

$$mv_x(\dot{\beta}+\psi) = F_{yf}+F_{yr}, \quad I_z\dot{\psi} = l_f F_{yf} - l_r F_{yr} \tag{1}$$

where m and I_z, are the mass and the yaw moment, v_x is the longitudinal velocity, β and ψ are vehicle sideslip angle and yaw rate, l_f and l_r are the distances from front and rear axle to the center of gravity. F_{yf} and F_{yr} are lateral tire force of

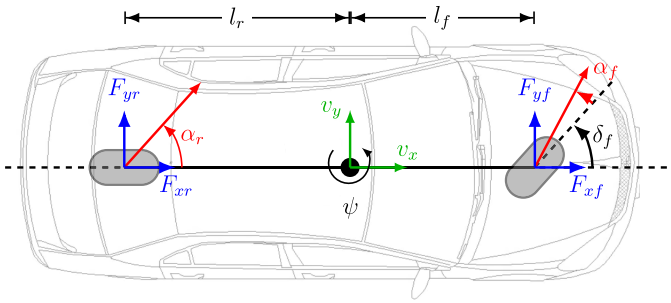

Fig. 1. The 2-DOF bicycle vehicle model.

front and rear tires, which can be modeled by the so-called Pacejka magic formula [37], with the assumption of small sideslip angle variations

$$F_{yf} = c_f\left(\delta_f - \beta - \frac{l_f}{v_x}\psi\right), F_{yr} = c_r\left(-\beta + \frac{l_r}{v_x}\psi\right) \quad (2)$$

where δ_f is the steering angle, c_f, c_r are the cornering stiffness of front and rear tires. Combining equations (1) and (2) and choosing β and ψ, as state variables, the following state-space model [38] can be derived:

$$\begin{bmatrix}\dot{\beta}\\ \dot{\psi}\end{bmatrix} = \begin{bmatrix} -\frac{c_f + c_r}{m v_x} & \frac{c_r l_r - c_f l_f}{m v_x^2} - 1 \\ \frac{c_r l_r - c_f l_f}{I_z} & -\frac{c_r l_r^2 + c_f l_f^2}{I_z v_x}\end{bmatrix}\begin{bmatrix}\beta\\ \psi\end{bmatrix} + \begin{bmatrix}\frac{c_f}{m v_x}\\ \frac{c_f l_f}{Iz}\end{bmatrix}\delta_f \quad (3)$$

B. LPV Model

Since data from sensors is obtained in a discrete-time manner, we will discretize the model (3) using Euler method with a sampling period T and defining the scheduling variable $\theta_k = [\frac{1}{v_x}, \frac{1}{v_x^2}]^T$. Then, the nonlinear vehicle model (3) can be equivalently transformed into the following discrete-time LPV model subject to disturbances and measurement noises,

$$x_{k+1} = A(\theta_k)x_k + B(\theta_k)u_k + Ew_k \quad (4a)$$
$$y_k = Cx_k + Fv_k \quad (4b)$$

with

$$x_k = \begin{bmatrix}\beta_k\\ \psi_k\end{bmatrix}, \quad u_k = \delta_{f_k}, \quad (5a)$$

$$A(\theta_k) = \begin{bmatrix} 1 - T\frac{c_f + c_r}{m v_x} & T\frac{c_r l_r - c_f l_f}{m {v_x}^2} - T \\ T\frac{c_r l_r - c_f l_f}{I_z} & 1 - T\frac{c_r l_r^2 + c_f l_f^2}{I_z v_x}\end{bmatrix}, \quad (5b)$$

$$B(\theta_k) = \begin{bmatrix} T\frac{c_f}{m v_x}\\ T\frac{c_f l_f}{Iz}\end{bmatrix}, \quad C = I. \quad (5c)$$

where $u_k \in \mathbb{R}^{n_u}$, $y_k \in \mathbb{R}^{n_y}$ and $x_k \in \mathbb{R}^{n_x}$ are the input, output and state vectors, respectively. Furthermore, disturbances and non-modelled effects are added to the vehicle model through additive state disturbance and measurement noise vectors $w_k \in \mathbb{R}^{n_w}$ and $v_k \in \mathbb{R}^{n_v}$, with constant distribution matrices $E \in \mathbb{R}^{n_x \times n_w}$ and $F \in \mathbb{R}^{n_y \times n_v}$. These uncertainties are assumed to be unknown but bounded by a unit hypercube expressed as the centered zonotopes, i.e., $w_k \in \mathcal{W} = \langle 0, I_{n_w}\rangle$ and $v_k \in \mathcal{V} = \langle 0, I_{n_v}\rangle$, where $I_{n_w} \in \mathbb{R}^{n_w \times n_w}$ and $I_{n_v} \in \mathbb{R}^{n_v \times n_v}$ denote the identity matrices. $A(\theta_k) \in \mathbb{R}^{n_x \times n_x}$, $B(\theta_k) \in \mathbb{R}^{n_x \times n_u}$ and $C \in \mathbb{R}^{n_y \times n_x}$ are the system matrices. These matrices depend on the vector of time-varying parameters $\theta_k \in \mathbb{R}^{n_\theta}$. θ_k varies over a fixed polytope Θ composed by its $N = 2^{n_\theta}$ vertices, n_θ represents the number of varying parameters. Considering the vertices of this polytope, the following polytopic form for the system matrices can be obtained: $A(\theta_k) = \sum_{i=1}^{N} \mu_i(\theta_k) A_i$, $B(\theta_k) = \sum_{i=1}^{N} \mu_i(\theta_k) B_i$, where $A_i \in \mathbb{R}^{n_x \times n_x}$, $B_i \in \mathbb{R}^{n_x \times n_u}$ for $i = 1, \ldots, N$ are known constant matrices. And $\mu(\cdot)$ is known as the vertex membership function, which satisfies

$$\sum_{i=1}^{N} \mu_i(\theta_k) = 1, \quad \mu_i(\theta_k) \geq 0, \ \forall \theta_k \in \Theta. \quad (6)$$

Then, the polytopic LPV form of (4) can be represented as follows:

$$x_{k+1} = \sum_{i=1}^{N} \mu_i(\theta_k)\left(A_i x_k + B_i u_k\right) + Ew_k \quad (7)$$

All the related parameters for the considered vehicle are listed in Table I.

TABLE I
MODEL PARAMETER VALUE

Parameter	Value	unit
l_f	1	m
l_r	1.44	m
m	1660	kg
c_f	35468	N/rad
c_r	40057	N/rad
I_z	2454	$kg.m^2$

III. SET-MEMBERSHIP BASED FDI

A. SMA for State Estimation

The monitoring of the AGVs is based on checking the consistency between the measurements and the estimated behaviours. This consistency check is based on the dynamic LPV model (4) using set-membership state estimation approach based on the prediction and correction steps through the following procedure [39]:

1) Prediction Step: Compute the uncertain state set $\overline{\mathcal{X}}_k$ at time instant k;
2) Measurement Step: Compute the measurement consistent state set $\mathcal{X}_{y_k}$ with the measured output y_k;
3) Correction Step: Compute an outer approximation $\hat{\mathcal{X}}_k$ of the intersection between $\overline{\mathcal{X}}_k$ and $\mathcal{X}_{y_k}$.

Based on the previous research [40], [41], the zonotopic SMA has been shown to be equivalent to a Current Zonotopic Observer. In this context, the SMA can be regarded as an

observer with the following structure:

$$\hat{x}_{k+1} = \sum_{i=1}^{N} \mu_i(\theta_k)(A_i\hat{x}_k + B_i u_k + \lambda_i \left(y_k - \hat{y}_k\right)) \tag{8a}$$

$$\hat{y}_k = C\hat{x}_k \tag{8b}$$

where $\hat{x} \in \mathbb{R}^{n_x}$ and $\hat{y} \in \mathbb{R}^{n_y}$ represent the estimated state and output vectors, respectively. $\lambda_i \in \mathbb{R}^{n_x \times n_y}$ is the observer gain. Then, the following theorem is a practical implementation of the state estimation of LPV systems using the SMA.

Theorem 1 (LMI-Based SMA): The zonotopic estimated state is denoted by the bounding zonotope $\hat{\mathcal{X}}_k = \langle c_{x,k}, R_{x,k} \rangle \in \mathbb{R}^{n_x}$, where $c_{x,k} \in \mathbb{R}^{n_x}$ and $R_{x,k} \in \mathbb{R}^{n_x \times n_{R_{x,k}}}$ represent the center and shape matrix. Assume that the initial state $\hat{x}_0$ belongs to the set $\hat{\mathcal{X}}_0 = \langle c_{x,0}, R_{x,0} \rangle$, the estimated state can be propagated as follows:

$$c_{x,k} = \overline{c}_{x,k} + \sum_{i=1}^{N} \mu_i(\theta_{k-1})\lambda_i \left(y_k - C\overline{c}_{x,k}\right) \tag{9a}$$

$$R_{x,k} = \sum_{i=1}^{N} \mu_i(\theta_{k-1}) \left[(I - \lambda_i C)\, \overline{R}_{x,k} \quad -\lambda_i F\right] \tag{9b}$$

with

$$\overline{c}_{x,k} = \sum_{i=1}^{N} \mu_i(\theta_{k-1})(A_i c_{x,k-1} + B_i u_{k-1}) \tag{10a}$$

$$\overline{R}_{x,k} = \left[\sum_{i=1}^{N} \mu_i(\theta_{k-1}) A_i R_{x,k-1} \quad E\right] \tag{10b}$$

where the uncertain state is $\overline{\mathcal{X}}_k = \langle \overline{c}_{x,k}, \overline{R}_{x,k} \rangle$, the optimal parameter λ_i is obtained by solving the following LMI optimization problem offline with the aim of minimizing the Frobenius radius of the zonotope shape matrix $R_{x,k}$

$$\min \gamma \tag{11}$$

subject to:

$$\begin{bmatrix} \gamma I_{n_x} & I_{n_x} \\ I_{n_x} & \Upsilon \end{bmatrix} > 0 \tag{12}$$

$$\begin{bmatrix} -\Upsilon & \Upsilon A_i - W_i C & \Upsilon E & W_i \\ A_i^T \Upsilon - C^T W_i^T & -\Upsilon & 0 & 0 \\ E^T \Upsilon & 0 & -I & 0 \\ W_i^T & 0 & 0 & -R^{-1} \end{bmatrix} < 0, \tag{13}$$

where $i = 1, \cdots, N$. $R = R^\top > 0$ is the covariance matrices of noise.

If there exist positive scalars γ, $\Upsilon = \Upsilon^\top$ and $W_i, i = 1, \cdots, N$, the optimal parameter λ_i per each vertex of the polytopic model can be obtained by solving the previous optimization problem:

$$\lambda_i = \Upsilon^{-1} W_i \tag{14}$$

Proof: A detailed proof is available in our previous work [42]. □

Remark 1: It is worth noting that the proposed method to calculate the optimal observer gain is different from a similar work [22] for Takagi-Sugeno systems, where the optimal observer gain is obtained by minimizing F-radius of the state bounding zonotope $\langle c_{x,k}, R_{x,k} \rangle$ and given by an online explicit solution. By minimizing the same radius, this paper aims to compute the parameter-dependent optimal observer gain through offline solving an LMI-based optimization problem. Furthermore, the proposed offline LMI-based solution can guarantee the state bounding zonotope has non-increasing size in time.

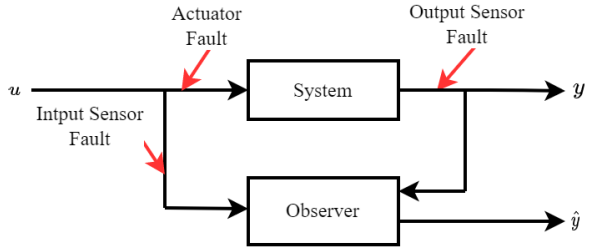

Fig. 2. Graphical interpretation of actuator and sensor faults.

B. SMA-Based FDI

As stated before, the FDI test consists of checking the consistency between the estimated and observed behaviors, where the consistency can be assessed by means of residuals given by

$$r_k = y_k - \hat{y}_k = y_k - C\hat{x}_k \tag{15}$$

Then, using Theorem 1, the zonotopic residual can be computed as

$$\begin{aligned} c_{r,k} &= y_k - C c_{x,k} \\ R_{r,k} &= -C R_{x,k} \end{aligned} \tag{16}$$

where $c_{r,k} \in \mathbb{R}^{n_y}$ and $R_{r,k} \in \mathbb{R}^{n_y \times n_{R_{r,k}}}$ represent the center and the generator matrix of the residual zonotope. Hence, faults can be detected by checking the satisfaction of

$$0 \notin \langle c_{r,k}, R_{r,k} \rangle. \tag{17}$$

IV. Characterization of MDF and MIF

SIA approach is based on propagating the state estimation error $\tilde{x}_k$, denoted by $\tilde{x}_k = x_k - \hat{x}_k$ and projecting $\tilde{x}_k$ to the residual space, where the residual will ultimately converge to an invariant set. Thus, the healthy and faulty invariant residual set can be obtained by operating SIA in each healthy or faulty operation mode of the system. Then, the MDF and MIF can be characterized by set separation.

Remark 2: In the faulty operation mode, several types of faults are considered according to their location as depicted in Fig.2. These include actuator faults which affect the system inputs, and sensor faults that affect the measurements of system inputs and outputs.

A. Invariant Residual Set Generation

Combining (4), (7) and (8), the dynamics of state estimation error can be defined as:

$$\tilde{x}_{k+1} = \sum_{i=1}^{N} \mu_i(\theta_k)((A_i - \lambda_i C)\tilde{x}_k - \lambda_i F v_k) + E w_k \tag{18}$$

The corresponding residual is generated as:

$$r_k = y_k - \hat{y}_k = C\tilde{x}_k + Fv_k \tag{19}$$

Here, we introduce some invariant set concepts [43] for further analysis.

Definition 1: A set $\tilde{\mathcal{X}}$ is an RPI set of the dynamics (18), if $\forall\theta_k \in \Theta$, $w_k \in \mathcal{W}$ and $v_k \in \mathcal{V}$, for any $\tilde{x}_k \in \tilde{\mathcal{X}}$, one has $\tilde{x}_{k+1} \in \tilde{\mathcal{X}}$.

Definition 2: The mRPI set of (18) is defined as a RPI set contained in any closed RPI set and the mRPI set is unique and compact.

1) Healthy Zonotopic mRPI Set: The healthy RPI set is propagated using zonotopes when the system (4) is operated in healthy mode. Then, the healthy mRPI set can be obtained in the steady state by the following theorem.

Theorem 2: Consider the state estimation error dynamics in (18), the zonotopic RPI set of the state estimation error $\tilde{\mathcal{X}}_k = \langle c_{\tilde{x}_k}, R_{\tilde{x}_k}\rangle \in \mathbb{R}^{n_x}$ can be propagated as

$$\begin{aligned} c_{\tilde{x}_{k+1}} &= \sum_{i=1}^{N} \mu_i(\theta_k)(A_i - \lambda_i C)\, c_{\tilde{x}_k}, \\ R_{\tilde{x}_{k+1}} &= \sum_{i=1}^{N} \mu_i(\theta_k)\begin{bmatrix}(A_i - \lambda_i C) R_{\tilde{x}_k} & E & -\lambda_i F\end{bmatrix}, \end{aligned} \tag{20}$$

Then, in the steady state, when $k \to \infty$, the zonotopic mRPI set $\tilde{\mathcal{X}}_\infty$ can be written as $\tilde{\mathcal{X}}_\infty = \bigoplus_{i=0}^{\infty} \mathcal{A}^i(W)$, where $\mathcal{A}(\cdot)$ is the set mapping defined as $\mathcal{A}(W) = \boldsymbol{Conv}\left\{\bigcup_{i=1}^{N}(A_i - \lambda_i C) W\right\}$, $W = \langle 0, E\rangle \oplus \lambda(F)$ represents the uncertainties, where $\lambda(F) = \boldsymbol{Conv}\left\{\bigcup_{i=1}^{N} \lambda_i \langle 0, -F\rangle\right\}$.

Proof: Suppose that $\tilde{\mathcal{X}}_0$ is an initial zonotopic RPI set for (20), then based on [20], the sequence $\tilde{\mathcal{X}}_k$ can be propagated as follows:

$$\tilde{\mathcal{X}}_{k+1} = \mathcal{A}(\tilde{\mathcal{X}}_k) \oplus W = \mathcal{A}^k(\tilde{\mathcal{X}}_0) \oplus \sum_{i=1}^{k} \mathcal{A}^{i-1}(W)$$

It is also known that $\tilde{\mathcal{X}}_k$ describes a monotonic sequence of RPI set in terms of set inclusions, such as,

$$\tilde{\mathcal{X}}_\infty \subseteq \tilde{\mathcal{X}}_{k+1} \subseteq \tilde{\mathcal{X}}_k \subseteq \tilde{\mathcal{X}}_0.$$

Furthermore, considering $\lim_{k\to+\infty} \mathcal{A}^k(\tilde{\mathcal{X}}_0) = \mathbf{0}$, the zonotopic mRPI set of (20) is given by

$$\tilde{\mathcal{X}}_\infty = \lim_{k\to+\infty} \tilde{\mathcal{X}}_k = \bigoplus_{i=0}^{\infty} \mathcal{A}^i(W)$$

□

Therefore, the zonotopic invariant mRPI residual set in healthy situation is given by projecting the state estimation error into the residual space using (19)

$$\mathcal{R} = \langle R_c, R_r\rangle = C\tilde{\mathcal{X}}_\infty \oplus F\mathcal{V} \tag{21}$$

where R_c, R_r are the center and shape matrix of healthy invariant residual zonotopes $\mathcal{R}$.

Remark 3: Because of the infinite iterations required to obtain the mRPI set in Theorem 2, a finite recursive procedure based on an outer-approximation method with given precision [20] is considered to generate the mRPI set.

2) Faulty Zonotopic mRPI Set: In faulty operation mode of the system, the case of actuator and sensor faults is considered. Including their effect, the dynamic model (4) can be rewritten as follows:

$$x_{k+1} = A(\theta_k)x_k + B(\theta_k)(u_k + G_a f_a) + Ew_k \tag{22a}$$

$$y_k = Cx_k + Fv_k + G_y f_y \tag{22b}$$

where scalars f_a and f_y denote the actuator and output sensor faults with their associated known constant matrices $G_a \in \mathbb{R}^{n_u \times n_u}$ and $G_y \in \mathbb{R}^{n_y}$, respectively. Furthermore, input sensor fault is also considered with its effect on the input of the observer (8) as:

$$\hat{x}_{k+1} = \sum_{i=1}^{N} \mu_i(\theta_k)\left(A_i\hat{x}_k + B_i(u_k + G_u f_u) + \lambda_i\left(y_k - \hat{y}_k\right)\right) \tag{23}$$

where the scalar f_u represents input sensor fault with its associated known constant matrix $G_u \in \mathbb{R}^{n_u \times n_u}$.

Then, the dynamics of state estimation error in faulty scenario with the considered actuator, input and output sensor faults is modeled as follows:

$$\tilde{x}_{k+1}^{f,d} = \sum_{i=1}^{N} \mu_i(\theta_k)\left((A_i - \lambda_i C)\tilde{x}_k^{f,d} - \lambda_i F v_k\right) + Gf + Ew_k \tag{24}$$

where

$$G = \sum_{i=1}^{N} \mu_i(\theta_k)\begin{bmatrix}B_i G_a & -\lambda_i G_y & -B_i G_u\end{bmatrix}, \tag{25a}$$

$$f = \begin{bmatrix}f_a & f_y & f_u\end{bmatrix}^T. \tag{25b}$$

Remark 4: It is worth mentioning that when MDF/MIF analysis is performed, only one fault is considered at the same time in the system (24), e.g., in the case of an actuator fault, $G = \sum_{i=1}^{N} \mu_i(\theta_k) B_i G_a$ and $f = f_a$.

Theorem 3: The zonotopic RPI set of the faulty state estimation error (24), denoted by $\tilde{\mathcal{X}}_k^{f,d} = \left\langle c_{\tilde{x}_k^{f,d}}, R_{\tilde{x}_k^{f,d}}\right\rangle \in \mathbb{R}^{n_x}$, can be decomposed into disturbance and fault effects based on the superposition principle:

$$\tilde{\mathcal{X}}_k^{f,d} = \langle c_{\tilde{x}_k}, R_{\tilde{x}_k}\rangle \oplus \left\langle c_{\tilde{x}_k^f}, R_{\tilde{x}_k^f}\right\rangle \tag{26}$$

with

$$c_{\tilde{x}_{k+1}^f} = \sum_{i=1}^{N} \mu_i(\theta_k)(A_i - \lambda_i C)\, c_{\tilde{x}_k^f} + Gf, \tag{27a}$$

$$R_{\tilde{x}_{k+1}^f} = \sum_{i=1}^{N} \mu_i(\theta_k)(A_i - \lambda_i C)\, R_{\tilde{x}_k^f}, \tag{27b}$$

where $c_{\tilde{x}_{k+1}^f}$ and $R_{\tilde{x}_{k+1}^f}$ represent the zonotope state estimation error center and generator matrix due to the fault effects.

Therefore, when $k \to \infty$, the zonotopic faulty mRPI set $\tilde{\mathcal{X}}_{\infty}^{f,d}$ is obtained as follows:

$$\tilde{\mathcal{X}}_{\infty}^{f,d} = \tilde{\mathcal{X}}_{\infty} \oplus \tilde{\mathcal{X}}_{\infty}^{f} \tag{28}$$

where $\tilde{\mathcal{X}}_{\infty}^{f} = \bigoplus_{i=0}^{\infty} \mathcal{A}^{i}(G)$ denotes the mRPI set of the dynamics (27) in the case of $f = 1$.

Proof: The proof follows the same lines as Theorem 2. □

In case of actuator/input sensor fault, the zonotopic invariant mRPI residual set is obtained using the projection of equation (19) as follows: $\mathcal{R}^{f,d} = C\tilde{\mathcal{X}}_{\infty}^{f,d} \oplus F\mathcal{V} = \mathcal{R} \oplus fC\tilde{\mathcal{X}}_{\infty}^{f}$. Besides, it is worth noting that the residual dynamics under the case of output sensor fault is as follows:

$$r_k = y_k - \hat{y}_k = C\tilde{x}_k + Fv_k + G_y f_y \tag{29}$$

Hence, the zonotopic mRPI residual set in case of output sensor fault is $\mathcal{R}^{f,d} = \mathcal{R} \oplus Cf_y\tilde{\mathcal{X}}_{\infty}^{f} \oplus \{G_y f_y\} = \mathcal{R} \oplus f_y(C\tilde{\mathcal{X}}_{\infty}^{f} \oplus \{G_y\})$.

As under these two scenarios, the faulty mRPI residual set can be represented by the combination of the healthy invariant residual set $\mathcal{R}$ and the fault-caused invariant residual set. In the rest of the paper, the general notation $\mathcal{R}^{f,d} = \left\langle R_c^{f,d}, R_r^{f,d} \right\rangle = \mathcal{R} \oplus \mathcal{R}^{f}$ is adopted, where $\mathcal{R}^{f}$ represents the invariant zonotopic set caused by faults. Therefore, it refers to $fC\tilde{\mathcal{X}}_{\infty}^{f}$ in case of actuator/input sensor fault and $f_y(C\tilde{\mathcal{X}}_{\infty}^{f} \oplus \{G_y\})$ in case of output sensor fault. For simplification of the following computation, it is denoted by $\mathcal{R}^{f} = f\left\langle R_c^{f}, R_r^{f} \right\rangle$, where R_c^{*}, R_r^{*} are the center and shape matrix of corresponding residual zonotopes.

B. Detectability and Isolability Conditions

As known, in the faulty scenario the residual r_k will ultimately converge to the faulty mRPI residual set $\mathcal{R}^{f,d}$. Thus, the detectability condition yields to check if the intersection between the faulty and healty residual set is empty, i.e., $\mathcal{R} \cap \mathcal{R}^{f,d} = \emptyset$.

Following the detectability condition, the isolability condition needs to guarantee the isolation of a fault f_p from another fault f_q. Similarly, the condition is based on checking whether the intersection between the faulty residual set $\mathcal{R}^{f_p,d}$ of f_p and the other faulty residual set $\mathcal{R}^{f_q,d}$ of f_q is empty, i.e., $\mathcal{R}^{f_p,d} \cap \mathcal{R}^{f_q,d} = \emptyset$.

C. Computation of MDF and MIF

As known, the magnitudes of MDF and MIF are important criteria to assess the performance of fault detection. This subsection proposes two set-separation theorems to obtain the magnitude of MDF and MIF theoretically, instead of performing a lot of simulation tests, as used in conventional methods.

In order to compute the magnitude of MDF, we reformulate the constraint $\mathcal{R} \cap \mathcal{R}^{f,d} = \emptyset$ to an optimization problem [20] of the form:

$$\min_{f>0} f \quad \text{s.t. } \mathcal{R} \cap \mathcal{R}^{f,d} = \emptyset \tag{30}$$

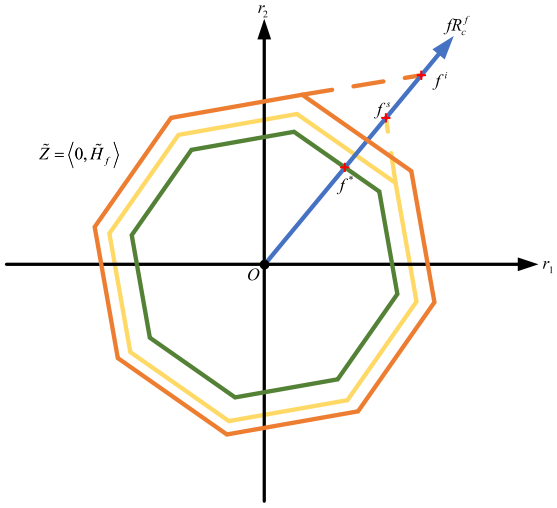

Fig. 3. Intersection point of problem (32) for the case of $n_y = 2, \tilde{m} = 4$, the orange, yellow and green polygons represent the centred zonotope $\tilde{\mathcal{Z}}$, whose size changes along with the magnitude of f. The blue arrow denotes the vector fR_c^f in the direction of $\vec{R}_c^f$. The intersection points between the zonotope and the vector are marked by the red **x**.

For simplicity, only the situation $f > 0$ is considered, since $f < 0$ can be handled equivalently by

$$\min_{f<0} -f \quad \text{s.t. } \mathcal{R} \cap \mathcal{R}^{f,d} = \emptyset. \tag{31}$$

Recalling that $\mathcal{R} = \langle R_c, R_r \rangle$, $\mathcal{R}^{f,d} = \left\langle R_c + fR_c^f, R_r^{f,d} \right\rangle$, based on Lemma 2 in the Appendix, the intersection (30) is empty if and only if

$$\begin{aligned}
&R_c - R_c \notin \langle \mathbf{0}, R_r \rangle \oplus \left\langle -fR_c^f, R_r^{f,d} \right\rangle \\
&\quad \Leftrightarrow \mathbf{0} \notin \langle \mathbf{0}, R_r \rangle \oplus \left\{ -fR_c^f \right\} \oplus \left\langle \mathbf{0}, fR_r^f \right\rangle \oplus \langle \mathbf{0}, R_r \rangle \\
&\quad \Leftrightarrow fR_c^f \notin \langle \mathbf{0}, R_r \rangle \oplus \langle \mathbf{0}, R_r \rangle \oplus \left\langle \mathbf{0}, fR_r^f \right\rangle \\
&\quad \Leftrightarrow fR_c^f \notin \langle \mathbf{0}, H \rangle \oplus f\left\langle \mathbf{0}, \bar{H} \right\rangle \\
&\quad \Leftrightarrow fR_c^f \notin \left\langle \mathbf{0}, \tilde{H}_f \right\rangle
\end{aligned}$$

where $H = 2R_r \in \mathbb{R}^{n_y \times m}$, $\bar{H} = R_r^f \in \mathbb{R}^{n_y \times \tilde{m}}$, $\tilde{H}_f = \begin{bmatrix} H & f\bar{H} \end{bmatrix} \in \mathbb{R}^{n_y \times \tilde{m}}$, $\tilde{m} = m + \tilde{m}$. Hereby, the optimization problem is equal to

$$\min_{f>0} f \quad \text{s.t. } fR_c^f \notin \left\langle \mathbf{0}, \tilde{H}_f \right\rangle \tag{32}$$

Solving the above optimization problem is equivalently transformed into searching the intersection point between the vector fR_c^f and the zonotope $\tilde{\mathcal{Z}} = \left\langle \mathbf{0}, \tilde{H}_f \right\rangle$ as shown in Fig. 3. As f increases, there exist several intersection points (the red x mark in Fig. 3), which correspond to different f magnitudes (e.g., f^*, f^s, f^i). Among them, the minimum intersection point f^* is the desired MDF. In order to compute the intersection point, the zonotope $\tilde{\mathcal{Z}}$ has to be transformed into the half-space representation using the following lemma.

Lemma 1: Based on the Lemma 3 given in Appendix, let $Z = \langle g, H_t \rangle \subseteq \mathbb{R}^n$ be the the Minkowski sum of two centered zonotopes $Z_1 = \langle g_1, H_1 \rangle \subseteq \mathbb{R}^n$, $Z_2 = t\langle g_2, H_2 \rangle \subseteq \mathbb{R}^n$, where

$g = g_1 + tg_2$, $H_t = [H_1 \quad tH_2] = \left[\tilde{h}_1, \ldots, \tilde{h}_m\right] \in \mathbb{R}^{n\times m}$, $H_1 = \left[h_1, \ldots, h_{m_1}\right] \in \mathbb{R}^{n\times m_1}$, $H_2 = \left[h_{m_1+1}, \ldots, h_m\right] \in \mathbb{R}^{n\times m_2}$, $m = m_1 + m_2$ *and* t *is a scalar. Then, the halfspace representation* $\mathcal{H}(Z) = \{x \in \mathbb{R}^n \mid \mathcal{A}x \le \mathcal{B}\}$ *of* Z *can be written as*

$$\mathcal{A} = \begin{bmatrix} \mathcal{A}^+ \\ -\mathcal{A}^+ \end{bmatrix}, \quad \mathcal{B} = \begin{bmatrix} \mathcal{B}^+ \\ \mathcal{B}^- \end{bmatrix} \tag{33}$$

where

$$\begin{aligned}
\mathcal{A}_s^+ &= \frac{\mathbf{nX}\left(H^{\langle\gamma,\ldots,\eta\rangle}\right)^T}{\left\|\mathbf{nX}\left(H^{\langle\gamma,\ldots,\eta\rangle}\right)\right\|_2}, \quad H = [H_1 \quad H_2], \\
\mathcal{B}_s^+ &= \mathcal{B}_{1s}^+ + \mathcal{B}_{2s}^+, \quad \mathcal{B}_s^- = \mathcal{B}_{1s}^- + \mathcal{B}_{2s}^-, \\
\mathcal{B}_{1s}^+ &= \mathcal{A}_s^+ g_1 + \Delta\mathcal{B}_{1s}, \quad \mathcal{B}_{2s}^+ = t\mathcal{A}_s^+ g_2 + |t|\,\Delta\mathcal{B}_{2s}, \\
\mathcal{B}_{1s}^- &= -\mathcal{A}_s^+ g_1 + \Delta\mathcal{B}_{1s}, \quad \mathcal{B}_{2s}^- = -t\mathcal{A}_s^+ g_2 + |t|\,\Delta\mathcal{B}_{2s}, \\
\Delta\mathcal{B}_{1s} &= \sum_{j=1}^{m_1} \left|\mathcal{A}_s^+ h_j\right|, \quad \Delta\mathcal{B}_{2s} = \sum_{j=m_1+1}^{m} \left|\mathcal{A}_s^+ h_j\right|.
\end{aligned} \tag{34}$$

with the same symbol notations as that of Lemma 3 in Appendix.

Proof: Based on Lemma 3 in Appendix, $\mathcal{A}_s^+ = \frac{\mathbf{nX}\left(H_t^{\langle\gamma,\ldots,\eta\rangle}\right)^T}{\left\|\mathbf{nX}\left(H_t^{\langle\gamma,\ldots,\eta\rangle}\right)\right\|_2}$, $\mathcal{B}_s^+ = \mathcal{A}_s^+ g + \Delta\mathcal{B}_s = \mathcal{A}_s^+ g + \sum_{j=1}^{m}\left|\mathcal{A}_s^+ \tilde{h}_j\right|$. Assuming that

$$H_t^{\langle\gamma,\ldots,\eta\rangle} = \underbrace{[h_1, \ldots, h_k}_{n_1}, \underbrace{th_p, \ldots, t\ h_q]}_{n_2}$$

is composed by n_1 generators from Z_1 and n_2 generators from Z_2, where $n_1+n_2 = n-1$. Then, the cross product of $H_t^{\langle\gamma,\ldots,\eta\rangle}$ can be given as $\mathbf{nX}\left(H_t^{\langle\gamma,\ldots,\eta\rangle}\right) = t^{n_2}\mathbf{nX}\left(H^{\langle\gamma,\ldots,\eta\rangle}\right)$ with $det(H_t^{\langle\gamma,\ldots,\eta\rangle[i]}) = t^{n_2} det(H^{\langle\gamma,\ldots,\eta\rangle[i]})$. As a consequence, $\mathcal{A}_s^+ = \frac{t^{n_2}\mathbf{nX}(H^{\langle\gamma,\ldots,\eta\rangle})^T}{t^{n_2}\|\mathbf{nX}(H^{\langle\gamma,\ldots,\eta\rangle})\|_2} = \frac{\mathbf{nX}(H^{\langle\gamma,\ldots,\eta\rangle})^T}{\|\mathbf{nX}(H^{\langle\gamma,\ldots,\eta\rangle})\|_2}$.

Besides, it is easy to decompose the element $\mathcal{B}_s^+$ as two parts: $\mathcal{B}_{1s}^+ = \mathcal{A}_s^+ g_1 + \sum_{j=1}^{m1}\left|\mathcal{A}_s^+ \tilde{h}_j\right|$ and $\mathcal{B}_{2s}^+ = \mathcal{A}_s^+ tg_2 + \sum_{j=m_1+1}^{m}\left|\mathcal{A}_s^+ \tilde{h}_j\right|$, where $\tilde{h}_j = \begin{cases} h_j, 1 \le j \le m_1 \\ t \cdot h_j, m_1+1 \le j \le m \end{cases}$. Therefore, $\mathcal{B}_s^+$ can be organized into (34), $\mathcal{B}_s^-$ can be obtained similarly. □

Theorem 4: (MDF) The optimal solution f^* *for the MDF optimization problem is obtained by searching*

$$\begin{aligned}
f^* = &\min\{f^s\} \\
&subject\ to \\
&f^s = d_{1s}^+/(\left|\mathcal{A}_s^+ R_c^f\right| - d_{2s}^+),\ 1 \le s \le \binom{\tilde{m}}{n_y - 1}, \\
&\mathcal{A}_s^+ = \frac{\mathbf{nX}\left(\tilde{H}^{\langle\gamma,\ldots,\eta\rangle}\right)^T}{\left\|\mathbf{nX}\left(\tilde{H}^{\langle\gamma,\ldots,\eta\rangle}\right)\right\|_2}, \tilde{H} = [H \quad \bar{H}] \in \mathbb{R}^{n_y\times\tilde{m}}, \\
&d_{1s}^+ = \sum_{j=1}^{m}\left|\mathcal{A}_s^+ \tilde{h}_j\right|, d_{2s}^+ = \sum_{j=m+1}^{\tilde{m}}\left|\mathcal{A}_s^+ \tilde{h}_j\right|.
\end{aligned} \tag{35}$$

Proof: Based on Lemma 1, we can obtain the half-space representation of $\left\langle \mathbf{0}, \tilde{H}_f \right\rangle$, that is $\mathcal{H}(\left\langle \mathbf{0}, \tilde{H}_f \right\rangle) = \{x \in \mathbb{R}^{n_y} \mid \mathcal{A}x \le d\}$ with

$$\mathcal{A} = \begin{bmatrix} \mathcal{A}^+ \\ -\mathcal{A}^+ \end{bmatrix}, \quad d = \begin{bmatrix} d^+ \\ d^- \end{bmatrix} \tag{36}$$

where

$$\begin{aligned}
\mathcal{A}_s^+ &= \frac{\mathbf{nX}\left(\tilde{H}^{\langle\gamma,\ldots,\eta\rangle}\right)^T}{\left\|\mathbf{nX}\left(\tilde{H}^{\langle\gamma,\ldots,\eta\rangle}\right)\right\|_2}, \quad \tilde{H} = [H \quad \bar{H}], \\
d^+ &= d_1^+ + |f|\,d_2^+, \quad d^- = d^+, \\
d_1^+ &= \Delta d_{1s}, \quad d_2^+ = \Delta d_{2s}, \\
\Delta d_{1s} &= \sum_{j=1}^{m}\left|\mathcal{A}_s^+ \tilde{h}_j\right|, \quad \Delta d_{2s} = \sum_{j=m+1}^{\tilde{m}}\left|\mathcal{A}_s^+ \tilde{h}_j\right|,
\end{aligned}$$

Since $\mathcal{H}(\langle 0, \tilde{H}_f\rangle)$ is central symmetric, we only need to consider the intersection point in $m + \bar{m}$ half-space zonotope $\mathcal{H}^+(\langle 0, \tilde{H}_f\rangle) = \{r \in \mathbb{R}^{n_y} \mid \mathcal{A}^+ r \le d^+\}$. For each hyperplane $\left\{r \in \mathbb{R}^{n_y} \mid \mathcal{A}_s^+ r = d_s^+ = d_{1s}^+ + |f^s| d_{2s}^+\right\}$, considering that the point $f^s R_c^f$ is in the hyperplane $\left\{r \in \mathbb{R}^{n_y} \mid \mathcal{A}_s^+ r = d_{1s}^+ + |f^s| d_{2s}^+\right\}$, it follows $\mathcal{A}_s^+ f^s R_c^f = d_{1s}^+ + |f^s| d_{2s}^+$. Additionally, in the case of $f^s > 0$, it can be obtained that $f^s = d_{1s}^+/(\left|\mathcal{A}_s^+ R_c^f\right| - d_{2s}^+)$. Therefore, the optimal f^* could be obtained by choosing the minimum value among the set $\{f^s\}, 1 \le s \le \binom{\tilde{m}}{n_y - 1}$. □

Furthermore, in order to obtain the isolability of two faults, this paper proposes the following theorem to compute the MIF by extending Theorem 4. A graphical explanation is given for the following MIF theorem.

Theorem 5 (MIF): The MIF of a fault f_p *from another fault* f_q *can be determined by solving the following optimization problem*

$$\min f_p \quad s.t.\ \mathcal{R}^{f_p,d} \cap \mathcal{R}^{f_q,d} = \emptyset \tag{37}$$

Considering a similar transformation procedure as (32), this optimization problem is equal to

$$\min f_p \quad s.t.\ f_p R_c^{f_p} - f_q R_c^{f_q} \notin \left\langle \mathbf{0}, \tilde{H}_{f_{p,q}} \right\rangle \tag{38}$$

where $\tilde{H}_{f_{p,q}} = [H_1 \quad f_p H_2 \quad f_q H_3] \in \mathbb{R}^{n_y\times\tilde{m}}$, $H_1 = 2R_c \in \mathbb{R}^{n_y\times m_1}$, $H_2 = R_c^{f_p} \in \mathbb{R}^{n_y\times m_2}$, $H_3 = R_c^{f_p} \in \mathbb{R}^{n_y\times m_3}$, $f_p \in [\underline{f_p}, \overline{f_p}]$.

The optimal solution for the optimization problem (38) is given by

$$\begin{aligned}
&\underline{f_p} = \min\{f_p^*\}, \overline{f_p} = \max\{f_p^*\}, \\
&\{f_p^*\} = \{f_p^i \mid f_p^i R_c^{f_p} - f_q R_c^{f_q} \in \left\langle \mathbf{0}, \tilde{H}_{f_{p,q}^i} \right\rangle, f_p^i \in F_p\}.
\end{aligned} \tag{39}$$

where, $\tilde{H}_{f_{p,q}^i} = [H_1 \quad f_p^i H_2 \quad f_q H_3]$, $i = 1, \ldots, 2\tilde{m}$, $F_p = \{f_{p_1}^s\} \cup \{f_{p_2}^s\} = \{f_p^1, \ldots, f_p^{2\tilde{m}}\}$ *denotes the collection of the fault magnitudes satisfying the points* $f_{p_1}^s R_c^{f_p} - f_q R_c^{f_q}$, $f_{p_2}^s R_c^{f_p} - f_q R_c^{f_q}$ *are in the following hyperplane*:

$$f_{p_1}^s \mathcal{A}_s^+ R_c^{f_p} = d_{1s}^+ + |f_{p_1}^s| d_{2s}^+ + |f_q| d_{3s}^+ + \mathcal{A}_s^+ f_q R_c^{f_q}, \tag{40a}$$

$$f_{p_2}^s \mathcal{A}_s^- R_c^{f_p} = d_{1s}^+ + |f_{p_2}^s| d_{2s}^+ + |f_q| d_{3s}^+ + \mathcal{A}_s^- f_q R_c^{f_q}, \tag{40b}$$

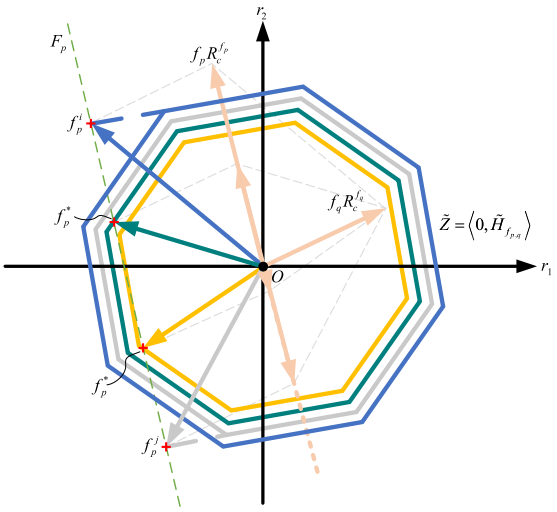

Fig. 4. Intersection point of problem (38) for the case of determining a minimum fault f_p that can be isolated from a known fault f_q, with $n_y = 2, \tilde{m} = 4$. The yellow, green, grey and blue polygons represent the centred zonotope $\tilde{\mathcal{Z}} = \langle \mathbf{0}, \tilde{H}_{f_{p,q}} \rangle$, whose size changes along with the magnitude of f_p. The light pink arrow denotes the vector $f_p R_c^{f_p}$ and $f_q R_c^{f_q}$ in the direction of $\overrightarrow{R}_c^{f_p}$ and $\overrightarrow{R}_c^{f_q}$, respectively. The vector difference $f_p R_c^{f_p} - f_q R_c^{f_q}$ is represented by the yellow, green, grey and blue arrows. The intersection points between the zonotope and the vector difference are marked by the red **x**, which consist of the fault magnitude set F_p in green dashed line.

where

$$\mathcal{A}_s^+ = \frac{\mathbf{nX}\left(\tilde{H}^{\langle \gamma,\ldots,\eta \rangle}\right)^T}{\left\|\mathbf{nX}\left(\tilde{H}^{\langle \gamma,\ldots,\eta \rangle}\right)\right\|_2}, \quad \mathcal{A}_s^- = -\mathcal{A}_s^+,$$

$$\tilde{H} = [H_1 \quad H_2 \quad H_3] \in \mathbb{R}^{n_y \times \tilde{m}}, \quad 1 \leq s \leq \binom{\tilde{m}}{n_y - 1},$$

$$d_{1s}^+ = \sum_{j=1}^{m_1} \left| \mathcal{A}_s^+ \tilde{h}_j \right|, \quad d_{2s}^+ = \sum_{j=m_1+1}^{m_1+m_2} \left| \mathcal{A}_s^+ \tilde{h}_j \right|,$$

$$d_{3s}^+ = \sum_{j=m_1+m_2+1}^{\tilde{m}} \left| \mathcal{A}_s^+ \tilde{h}_j \right|.$$

Proof: The proof follows a similar procedure than the one used in Theorem 4. Considering the intersection point in each halfspace zonotope, i.e., $\mathcal{H}^+(\langle 0, \tilde{H}_{f_{p,q}} \rangle) = \{r \in \mathbb{R}^{n_y} \mid \mathcal{A}^+ r \leq d^+\}$ and $\mathcal{H}^-(\langle 0, \tilde{H}_{f_{p,q}} \rangle) = \{r \in \mathbb{R}^{n_y} \mid \mathcal{A}^- r \leq d^-\}$, we can obtain the corresponding fault magnitude set $F_p = \{f_p^i, f_p^j, f_p^*\}$ as shown in Fig. 4. While there are only two magnitude-corresponding points $f_p^* R_c^{f_p} - f_q R_c^{f_q}$ exactly contained in the zonotope $\left\langle \mathbf{0}, \tilde{H}_{f_{p,q}^*} \right\rangle$, which are the optimal solution. □

It is worth noting that the minimum magnitude of the fault that represents a fault is detectable when $f_{min}^D \notin [-f^*, f^*]$ and isolable if $f_{min}^I \notin [\underline{f_p}, \overline{f_p}]$ according to Theorem 4 and Theorem 5, respectively. Therefore, it can be written that in the case of satisfaction of both conditions in (30) and (37), i.e., $f_p \notin [-f^*, f^*] \cup [\underline{f_p}, \overline{f_p}]$, the fault f_p can be both detected and isolated.

Fig. 5. Test track.

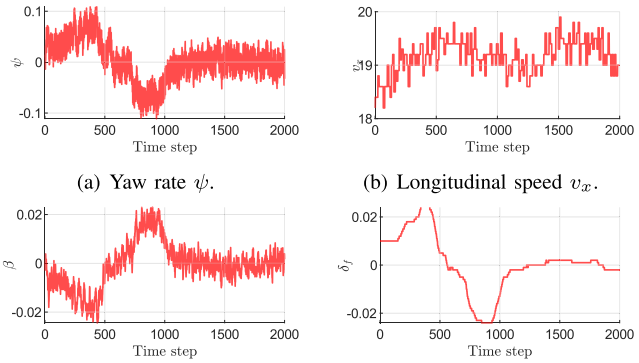

(a) Yaw rate ψ. (b) Longitudinal speed v_x.

(c) Sideslip angle β. (d) Steering angle δ_f.

Fig. 6. Figure of measurements.

V. Illustrative Results and Discussions

In this section, the SMA-based fault detection scheme designed in Section III and the SIA-based characterization method proposed in Section IV are applied to the fault detection problem of vehicle lateral dynamic system described in Section II. The real data used in the validation process are acquired using a prototype vehicle. The run was performed on a test track (Fig.5) located in the city of Versailles-Satory (France). The track is 3.5 km length with various curve profiles allowing vehicle dynamics excitation. Several sensors are installed in the vehicle. The yaw rate ψ is measured using an Inertial Measurement Unit (IMU). An odometer is used to provide the vehicle's longitudinal speed. The sideslip angle β is obtained using a Correvit sensor and the steering angle δ_f is measured by an absolute optical encoder. All the available measurements are depicted in Fig.6. The uncertainties considered in this paper are random noise bounded in zonotopes: $w \in \mathcal{W} = \langle 0, I_2 \rangle$ and $v \in \mathcal{V} = \langle 0, I_2 \rangle$, with the distribution matrices $E = \begin{bmatrix} 0.002 & 0 \\ 0 & 0.01 \end{bmatrix}$ and $F = \begin{bmatrix} 0.001 & 0 \\ 0 & 0.03 \end{bmatrix}$.

To perform the diagnosis scheme, an optimal observer is obtained by solving LMIs in Theorem 1. The obtained gains are given as follows:

$$\lambda_1 = \begin{bmatrix} 0.7764 & 0.0020 \\ -0.5485 & 0.2088 \end{bmatrix}, \quad \lambda_2 = \begin{bmatrix} 0.7913 & -0.0040 \\ -0.6893 & 0.3038 \end{bmatrix},$$

$$\lambda_3 = \begin{bmatrix} 0.4870 & 0.0039 \\ -0.1798 & 0.1884 \end{bmatrix}, \quad \lambda_4 = \begin{bmatrix} 0.6286 & 0.0060 \\ -0.2292 & 0.2142 \end{bmatrix}.$$

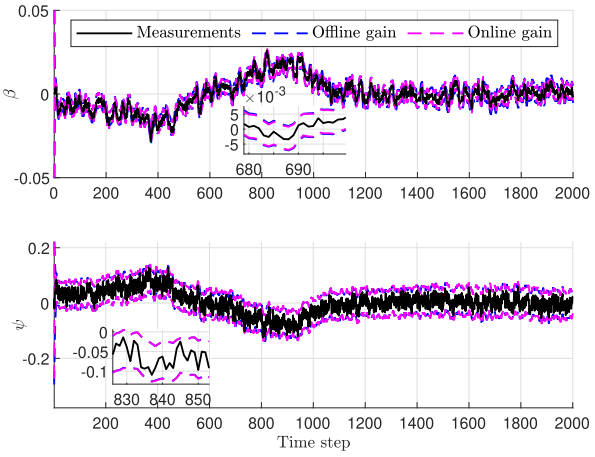

Fig. 7. Comparison of state estimation performance with the proposed SMA using offline observer gain and the zonotopic observer in [22] using online observer gain.

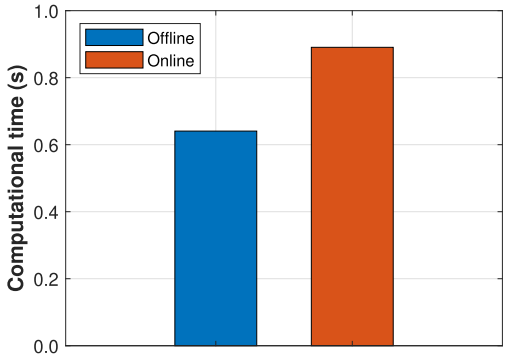

Fig. 8. Computation time required by each method.

To validate the estimation performance, a test scenario is performed when the system is working in its healthy mode. The state estimation is implemented using the proposed SMA, where the optimal observer gain is calculated offline by solving an LMI optimization problem, and the zonotopic observer proposed in [22], where the optimal observer gain is obtained online by an explicit solution. Fig. 7 shows the SMA provides satisfactory estimation results, and the equivalence between these two methods. Moreover, Fig. 8 reveals that the proposed offline SMA offers a more attractive solution from an implementation time-consumption point of view, in which experiments were conducted using an Intel Core i7 with a processor running at 2.8 GHz in MATLAB R2019b running under Windows 10. In contrast, the methodology employed by [22] involves online computation of observer gain, which is time-consuming. This distinction underscores the efficiency and practicality of our approach, especially in the context of vehicle applications.

A. Validation of Fault Detection

To illustrate the effectiveness of the SMA-based fault detection method, the following fault signals are considered for the steering actuator and yaw rate sensor, with their introduced matrices $G_a = 0.5$, $G_y = \begin{bmatrix} 0 \\ 1.3 \end{bmatrix}$. To validate actuator fault

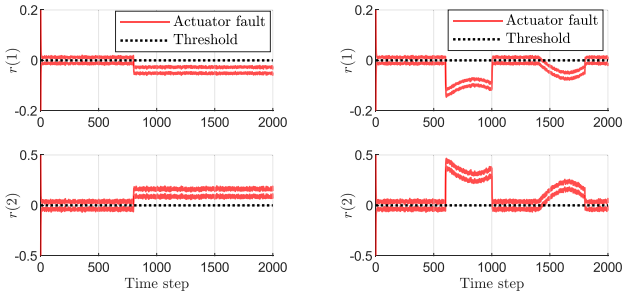

(a) SMA-based FD for f_{a1}. (b) SMA-based FD for f_{a2}.

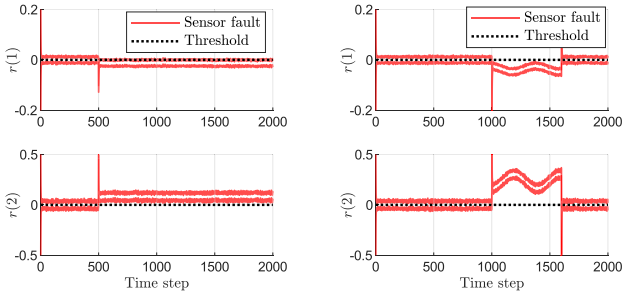

(c) SMA-based FD for f_{y_a}. (d) SMA-based FD for f_{y_b}.

Fig. 9. Fault detection results.

detection capability, two different faults are considered: A step fault f_{a1} and a time-varying fault f_{a2} are described as:

$$f_{a1}(k) = \begin{cases} 0 & k \leq 800 \\ 0.7 & 500 \leq k \end{cases}$$

$$f_{a2}(k) = \begin{cases} 1.5 - 0.5\sin(0.002\pi k) & 600 \leq k \leq 1000 \\ 0.7\sin(0.002\pi k - 2\pi) & 1400 \leq k \leq 1800 \\ 0 & elsewhere \end{cases}$$

For sensor fault detection test scenario, the following two typical faults are considered, e.g., a step fault f_{y_a} and a time-varying fault f_{y_b} are given as:

$$f_{y_a}(k) = \begin{cases} 0 & k \leq 500 \\ 0.7 & 500 \leq k \end{cases}$$

$$f_{y_b}(k) = \begin{cases} 2 - 0.6\cos(0.002\pi k) & 1000 \leq k \leq 1600 \\ 0 & elsewhere \end{cases}$$

Therefore, based on the SMA state estimation, FDI is performed by checking if the residuals are out of the threshold. The detection results are depicted in Fig.9, where the red solid line represents the upper and lower bound of the residual, and the black dotted line is the threshold. As we can see from the figure, both the actuator and sensor faults with different signals are detected immediately until they disappear and this is consistent with the theoretical analysis showing a good real-time detection performance.

B. MDF Analysis

As stated before, the characterization of MDF lies in the invariant set separation between healthy and faulty cases. In the following, the invariant sets are obtained based on SIA in different scenarios.

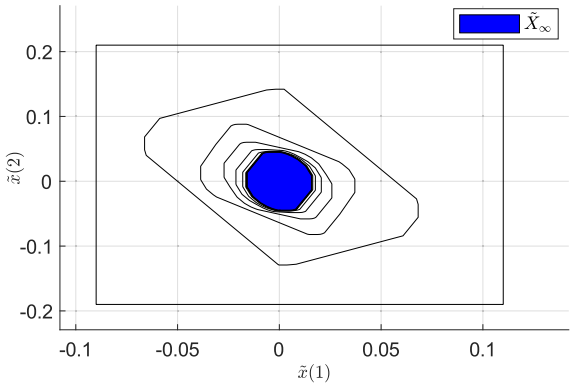

Fig. 10. Healthy mRPI set generation.

TABLE II
MAGNITUDE OF MDF

	f_a	f_u	f_{y_1}	f_{y_2}
MDF	± 0.2924	± 0.0975	± 0.3849	± 0.7208

1) Healthy Operation of the System: Given the polytopic LPV vehicle system (7), the considered states are the sideslip angle β and yaw rate ψ. Denoting the difference between the estimated and measured values by $\tilde{x}_1$ and $\tilde{x}_2$, the zonotopic RPI set of the state estimation error can be propagated at each time step using Theorem 2, depicted in Fig. 10. It can be seen that the zonotopic RPI set ultimately converges to the zonotopic mRPI set $\tilde{\mathcal{X}}_\infty$ (in blue). Then, the healthy invariant residual set $\mathcal{R}$ is obtained as shown in Fig. 11 by means of (21).

2) Faulty Operation of the System: In order to analyze the effect of different types of faults on the system and compute the magnitude of MDF during steady-state operation of the system, the faulty vehicle system (22) is given subject to actuator and sensor faults, i.e., actuator fault f_a, input sensor fault f_u, sideslip angle sensor fault f_{y_1} and yaw rate sensor fault f_{y_2}, introduced through the following matrices: $G_a = 0.5, G_u = 1.5$, $G_{y_1} = \begin{bmatrix} 0.4 \\ 0 \end{bmatrix}$ and $G_{y_2} = \begin{bmatrix} 0 \\ 1.3 \end{bmatrix}$, respectively.

In the following, by defining unit step actuator/sensor fault signals, the zonotopic RPI set of the state estimation error can be propagated as (26) and ultimately convergent to the zonotopic faulty mRPI set when the observer is becoming steady as $k \to \infty$. Then, the MDF can be characterised using Theorem 4. Following Section IV-C, the set separation results between the healthy and faulty mRPI residual sets with respect to the MDF of f_a, f_u, f_{y_1}, and f_{y_2} are shown in Fig. 11. The corresponding magnitudes of MDF are listed in Table II.

Consider the actuator fault as an example, with a greater magnitude than the MDF, given as:

$$f_a(k) = \begin{cases} 0 & k \leq 800 \\ 0.45 & 800 \leq k, \end{cases}$$

We can see that the healthy mRPI set and the faulty mRPI set are perfectly separated (see Fig. 12(b)), which indicates that this actuator fault is well detected. Furthermore, in terms

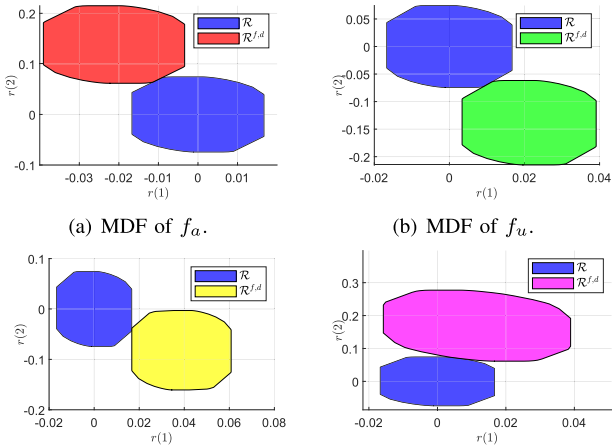

(a) MDF of f_a. (b) MDF of f_u.

(c) MDF of f_{y_1}. (d) MDF of f_{y_2}.

Fig. 11. Set-separation results between healthy and faulty invariant residual sets.

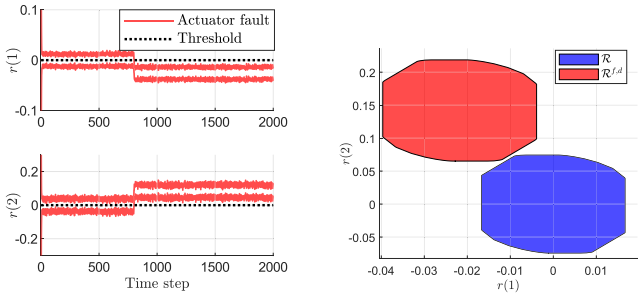

(a) SMA-based FD for f_a. (b) SIA-based FD for f_a.

Fig. 12. FD results in case of occurrence of the actuator fault f_a.

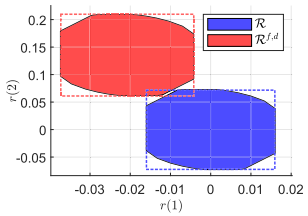

Fig. 13. SIA-based FD for f_a using intervals, the dashed line represents the interval mRPI set.

of SMA-based FDI, it is conducted for the actuator fault in both transient and steady states as shown in Fig. 12(a). It can be observed that SMA-based FDI could provide an earlier detection result, as it is obtained in the transient state. While SIA-based FDI provides the MDF/MIF results only when the system reaches the steady state. For this reason, this paper employs the SMA to perform the on-line fault diagnosis, and SIA to characterize the MDF and MIF. Moreover, using zonotopes to describe mRPI set can lead to a more compact set than using intervels [24], thus providing a more precise MDF magnitude, as described in Fig. 13. In the case of the same magnitude of fault, the zonotope sets are well separated, while the interval sets overlap. It can be concluded that using intervals normally leads to a larger MDF magnitude.

Furthermore, in order to validate the effectiveness of the MDF for other types of faults, a time-varying actuator fault and

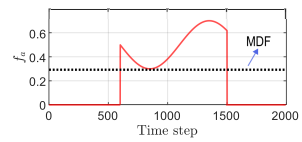

(a) Time-varying actuator fault.

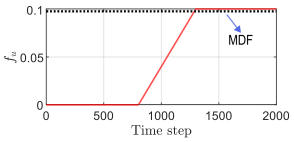

(b) Drift input sensor fault.

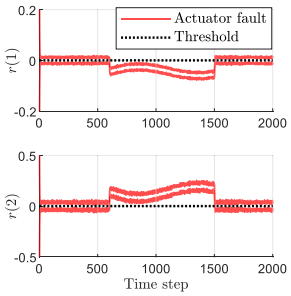

(c) Time-varying actuator fault detection.

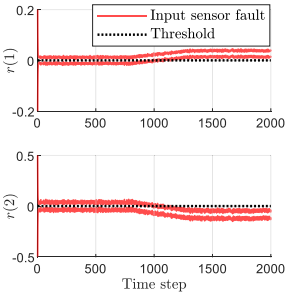

(d) Drift input sensor fault detection.

Fig. 14. Description of actuator and input sensor faults with their fault detection results.

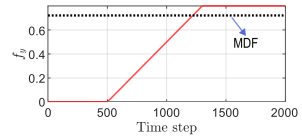

(a) Drift sensor fault with gentle slop.

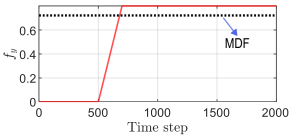

(b) Drift sensor fault with steep slop.

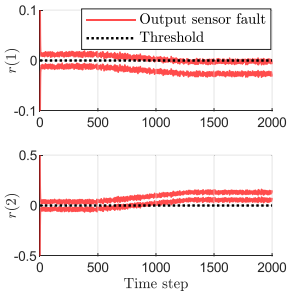

(c) Gentle drift output sensor fault detection.

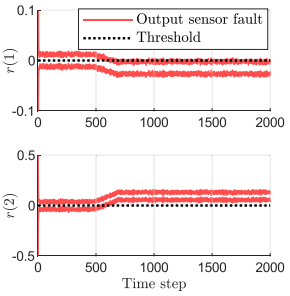

(d) Steep drift output sensor fault detection.

Fig. 15. Description of output sensor faults with their fault detection results.

drift sensor faults with slightly greater magnitudes than MDF are injected into actuator and sensor, respectively, described as Fig.14(a),14(b) and Fig.15(a),15(b). Notably, as drift faults are quite common on IMU, the comparisons (see Fig.15) are performed on drift faults with different slops. As observed from the detection results, depicted in Fig. 14(c),14(d) and Fig.15(c),15(d), the detection for abrupt fault is immediate, while for drift fault, a time delay appears and is related to the slope of the injected drift. In general, for any actuator or sensor fault, as long as their magnitudes are larger than the corresponding MDF, the detection can be guaranteed with the proposed SMA-based FDI method.

C. MIF Analysis

The above magnitude obtained using Theorem 4 is only related to detectability analysis while it is not valid in the case of isolability analysis, see Fig. 16(a). When the faults

TABLE III
MAGNITUDE OF MIF

	f_a	f_u	f_{y_1}	f_{y_2}
f_a^I	–	#	#	$[0.0059, 0.4730]$
f_u^I	#	–	$[0.0057, 0.1708]$	#
$f_{y_1}^I$	#	$[0.0052, 0.6468]$	–	#
$f_{y_2}^I$	$[0.0182, 1.1505]$	#	#	–

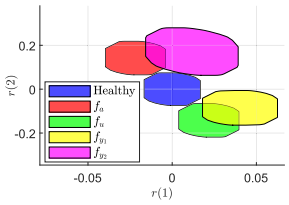

(a) Faults with slightly bigger magnitudes than MDF.

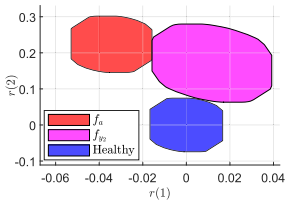

(b) Set-separation for the occurance of f_a and f_{y_2}.

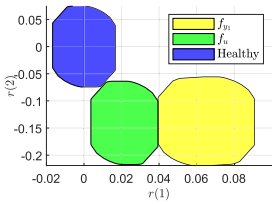

(c) Set-separation for the occurance of f_u and f_{y_1}.

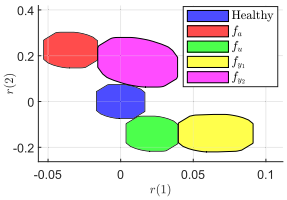

(d) Set-separation for all type of faults.

Fig. 16. Set-separation results between different faults.

are slightly greater than the corresponding MDF magnitudes, an overlap between the different faults is observed. Therefore, for the fault isolation purpose, the isolability condition of Theorem 5 must be satisfied.

Mainly, the implementation of MIF is done based on the MDF magnitudes reported in Table II as all faults are slightly bigger than the corresponding MDF magnitudes, i.e., $f_a = 0.299$, $f_u = 0.099$, $f_{y_1} = 0.40$ and $f_{y_2} = 0.73$. In this regard, the corresponding MIF magnitudes are reported on Table III, where the symbol $-$ in the table means that there are no corresponding cases in the considered study; the symbol # means that the faults are always isolable if they are larger than the MDF magnitude because these faults are in different directions. As is shown in Fig. 16(a), f_a and f_{y_2} can always be separated from f_u and f_{y_1} when they are larger than their corresponding MDF magnitudes. Moreover, with the magnitudes in Table III, the overlap between f_a and f_{y_2}, f_u and f_{y_1} can be perfectly avoided, as shown in Fig. 16(b) and 16(c), which proves the effectiveness of Theorem 5.

Besides, further analysis is done in the case of all types of possible faults occurring with slightly bigger magnitudes $f_a = 0.4750$, $f_u = 0.099$, $f_{y_1} = 0.65$ and $f_{y_2} = 0.73$ than the maximum MIF obtained in Table III. Fig. 16(d) presents the case of occurrence of the fault with the maximum value obtained in Table III, all type of faults are perfectly separated. This case corresponds to faults with magnitudes that are properly detectable and isolable.

VI. CONCLUSION

This paper has proposed a robust fault diagnosis algorithm using set-based approaches for LPV systems with application

to autonomous ground vehicles. First, a zonotope-based SMA with the optimal observer has been proposed for online fault detection, where the optimal observer gain is computed offline by solving an LMI optimization problem. This offline solution has been validated to be more time-saving facilitating the real-time implementation in a vehicle. Then, in order to characterise fault detectability and isolability, a zonotope-based SIA has been developed to obtain MDF and MIF by solving optimization problems subject to set separation conditions. In particular, this paper provides a simpler solution for the optimization problems by searching the intersection point. Furthermore, since a zonotopic description is employed, the magnitude of MDF/MIF is more precise than that of previous work. Finally, an application to autonomous ground vehicles is used in the case study to demonstrate the theoretical and practical interests of the proposed FDI scheme. In future work, authors plan to extend the proposed method for fault estimation and fault tolerant control problems with ground vehicle application.

APPENDIX

Lemma 2: Let $\mathcal{Z} = \langle a_z + b_z, H_z \rangle$ *and* $\mathcal{Y} = \langle a_y + b_y, H_y \rangle$. *Then,* $\mathcal{Z} \cap \mathcal{Y} = \emptyset$ *if and only if* $a_y - a_z \notin \langle b_z, H_z \rangle \oplus \langle -b_y, H_y \rangle$.

Lemma 3: The half-space representation [44] $\mathcal{H}(Z) = \{x \in \mathbb{R}^n \mid \mathcal{A}x \leq \mathcal{B}\}$ *of a zonotope* $Z = \langle g, H \rangle \subseteq \mathbb{R}^n$ *with* $H = [h_1, \ldots, h_m] \in \mathbb{R}^{n \times m}$ *is*

$$\mathcal{A} = \begin{bmatrix} \mathcal{A}^+ \\ -\mathcal{A}^+ \end{bmatrix}, \quad \mathcal{B} = \begin{bmatrix} \mathcal{B}^+ \\ \mathcal{B}^- \end{bmatrix}$$

where

$$\mathcal{A}_s^+ = \frac{\mathbf{nX}\left(H^{\langle \gamma, \ldots, \eta \rangle}\right)^T}{\left\| \mathbf{nX}\left(H^{\langle \gamma, \ldots, \eta \rangle}\right) \right\|_2}, \quad \mathcal{B}_s^+ = \mathcal{A}_s^+ g + \Delta\mathcal{B}_s,$$

$$\mathcal{B}_s^- = -\mathcal{A}_s^+ g + \Delta\mathcal{B}_s, \quad \Delta\mathcal{B}_s = \sum_{j=1}^{m} \left| \mathcal{A}_s^+ h_j \right|.$$

where $\mathcal{A}_s^+, \mathcal{B}_s^+$ *and* $\mathcal{B}_s^-$ *denote the* s*-th row of* $\mathcal{A}^+, \mathcal{B}^+$ *and* $\mathcal{B}^-$, *respectively; the index* s *varies from 1 to* $\binom{m}{n-1}$ *and the indices* $\gamma, \ldots, \eta$ *are the* $m - (n-1)$ *indices of the generators that are taken out of* H; $H^{\langle \gamma, \ldots, \eta \rangle} \in \mathbb{R}^{n \times (n-1)}$ *denotes matrix* H *where the columns indexed by* $\gamma, \ldots, \eta$ *are removed. The cross product operator can be defined as* $\mathbf{nX}(H) = \left[\ldots, (-1)^{i+1} det(H^{[i]}), \ldots\right]$, *and* $H^{[i]}$ *is defined as the matrix* H *in which the* i*-th row is removed.*

Lemma 4: A hyperplane $\mathcal{S} = \left\{x : c^T x = q\right\}$ *is a supporting hyperplane of a zonotope* $\mathcal{X} = \langle p, H \rangle$ *if either* $c^T x \leq \overline{q}, \forall x \in \mathcal{X}$ *or else* $c^T x \geq \underline{q}, \forall x \in \mathcal{X}$ *with equality occurring for some* $x \in \mathcal{X}$. *The two constants* $\overline{q}$ *and* $\underline{q}$ *characterizing the supporting hyperplanes are easily calculated as*

$$\overline{q} = c^T p + \left\| H^T c \right\|_1$$

$$\underline{q} = c^T p - \left\| H^T c \right\|_1$$

where $\| \cdot \|_1$ *is the 1-norm of a vector.*

REFERENCES

[1] K. Bengler, K. Dietmayer, B. Farber, M. Maurer, C. Stiller, and H. Winner, "Three decades of driver assistance systems: Review and future perspectives," *IEEE Intell. Transp. Syst. Mag.*, vol. 6, no. 4, pp. 6–22, Winter 2014.

[2] S. Cheng, L. Li, H.-Q. Guo, Z.-G. Chen, and P. Song, "Longitudinal collision avoidance and lateral stability adaptive control system based on MPC of autonomous vehicles," *IEEE Trans. Intell. Transp. Syst.*, vol. 21, no. 6, pp. 2376–2385, Jun. 2020.

[3] S. Ifqir, I. Dalil, A.-O. Naïma, and M. Saïd, "Adaptive threshold generation for vehicle fault detection using switched T–S interval observers," *IEEE Trans. Ind. Electron.*, vol. 67, no. 6, pp. 5030–5040, Jun. 2020.

[4] A. H. Tahoun, "Time-varying multiplicative/additive faults compensation in both actuators and sensors simultaneously for nonlinear systems via robust sliding mode control scheme," *J. Franklin Inst.*, vol. 356, no. 1, pp. 103–128, Jan. 2019.

[5] Y. Wang, L. Xu, F. Zhang, H. Dong, Y. Liu, and G. Yin, "An adaptive fault-tolerant EKF for vehicle state estimation with partial missing measurements," *IEEE/ASME Trans. Mechatronics*, vol. 26, no. 3, pp. 1318–1327, Jun. 2021.

[6] R. Rajamani, A. S. Howell, C. Chen, J. K. Hedrick, and M. Tomizuka, "A complete fault diagnostic system for automated vehicles operating in a platoon," *IEEE Trans. Control Syst. Technol.*, vol. 9, no. 4, pp. 553–564, Jul. 2001.

[7] J. Luo, M. Namburu, K. R. Pattipati, L. Qiao, and S. Chigusa, "Integrated model-based and data-driven diagnosis of automotive antilock braking systems," *IEEE Trans. Syst. Man, Cybern. A, Syst. Humans*, vol. 40, no. 2, pp. 321–336, Mar. 2010.

[8] N. Meskin and K. Khorasani, *Fault Detection and Isolation: Multi-Vehicle Unmanned Systems*. Cham, Switzerland: Springer, 2011.

[9] S. Varrier, D. Koenig, and J. J. Martinez, "Robust fault detection for vehicle lateral dynamics," in *Proc. IEEE 51st IEEE Conf. Decis. Control (CDC)*, Dec. 2012, pp. 4366–4371.

[10] S. Varrier, D. Koenig, and J. J. Martinez, "A parity space-based fault detection on LPV systems: Approach for vehicle lateral dynamics control System*," *IFAC Proc. Volumes*, vol. 45, no. 20, pp. 1191–1196, Jan. 2012.

[11] S. A. Arogeti, D. Wang, C. B. Low, and M. Yu, "Fault detection isolation and estimation in a vehicle steering system," *IEEE Trans. Ind. Electron.*, vol. 59, no. 12, pp. 4810–4820, Dec. 2012.

[12] C. Svärd, M. Nyberg, E. Frisk, and M. Krysander, "Data-driven and adaptive statistical residual evaluation for fault detection with an automotive application," *Mech. Syst. Signal Process.*, vol. 45, no. 1, pp. 170–192, Mar. 2014.

[13] D. Jung and E. Frisk, "Residual selection for fault detection and isolation using convex optimization," *Automatica*, vol. 97, pp. 143–149, Nov. 2018.

[14] J. Pan, A.-T. Nguyen, T.-M. Guerra, C. Sentouh, S. Wang, and J.-C. Popieul, "Vehicle actuator fault detection with finite-frequency specifications via Takagi–Sugeno fuzzy observers: Theory and experiments," *IEEE Trans. Veh. Technol.*, vol. 72, no. 1, pp. 407–417, Jan. 2023.

[15] X. Hu, Y. Che, X. Lin, and Z. Deng, "Health prognosis for electric vehicle battery packs: A data-driven approach," *IEEE/ASME Trans. Mechatronics*, vol. 25, no. 6, pp. 2622–2632, Dec. 2020.

[16] K. Zhang, B. Jiang, X.-G. Yan, and Z. Mao, "Incipient fault detection for traction motors of high-speed railways using an interval sliding mode observer," *IEEE Trans. Intell. Transp. Syst.*, vol. 20, no. 7, pp. 2703–2714, Jul. 2019.

[17] Y. Ma, Z. Nie, S. Hu, Z. Li, R. Malekian, and M. Sotelo, "Fault detection filter and controller co-design for unmanned surface vehicles under DoS attacks," *IEEE Trans. Intell. Transp. Syst.*, vol. 22, no. 3, pp. 1422–1434, Mar. 2021.

[18] J. Chen and R. J. Patton, *Robust Model-Based Fault Diagnosis For Dynamic Systems*, New York, NY, USA: Springer 1999.

[19] D. Eriksson, E. Frisk, and M. Krysander, "A method for quantitative fault diagnosability analysis of stochastic linear descriptor models," *Automatica*, vol. 49, no. 6, pp. 1591–1600, 2013.

[20] J. Tan, S. Olaru, M. Roman, F. Xu, and B. Liang, "Invariant set-based analysis of minimal detectable fault for discrete-time LPV systems with bounded uncertainties," *IEEE Access*, vol. 7, pp. 152564–152575, 2019.

[21] C. Zammali, J. Van Gorp, Z. Wang, X. Ping, and T. Raïssi, "Ellipsoid-based sensor fault detection for discrete-time switched systems," in *Proc. 59th IEEE Conf. Decis. Control (CDC)*, Dec. 2020, pp. 3267–3272.

[22] M. Pourasghar, A.-T. Nguyen, and T.-M. Guerra, "Zonotopic observer designs for uncertain Takagi–Sugeno fuzzy systems," *Eng. Appl. Artif. Intell.*, vol. 114, Sep. 2022, Art. no. 105126.
[23] S. Zhang, V. Puig, and S. Ifqir, "Zonotopic set-membership state estimation for switched LPV systems," *IFAC-PapersOnLine*, vol. 56, no. 2, pp. 9442–9447, 2023.
[24] M. Pourasghar, V. Puig, and C. Ocampo-Martinez, "Characterisation of interval-observer fault detection and isolation properties using the set-invariance approach," *J. Franklin Inst.*, vol. 357, no. 3, pp. 1853–1886, 2020.
[25] M. M. Seron, X. W. Zhuo, J. A. De Doná, and J. J. Martínez, "Multisensor switching control strategy with fault tolerance guarantees," *Automatica*, vol. 44, no. 1, pp. 88–97, Jan. 2008.
[26] C. Ocampo-Martinez, J. A. De Doná, and M. Seron, "Actuator fault-tolerant control based on set separation," *Int. J. Adapt. Control Signal Process.*, vol. 24, no. 12, pp. 1070–1090, 2010.
[27] F. Blanchini and S. Miani, *Set-Theoretic Methods in Control*, vol. 78. Cham, Switzerland: Springer, 2008.
[28] S. Olaru, J. A. De Doná, M. M. Seron, and F. Stoican, "Positive invariant sets for fault tolerant multisensor control schemes," *Int. J. Control*, vol. 83, no. 12, pp. 2622–2640, 2010.
[29] F. Stoican and S. Olaru, *Set-Theoretic Fault-Tolerant Control Multisensor Systems*. Hoboken, NJ, USA: Wiley, 2013.
[30] E. Kofman, H. Haimovich, and M. M. Seron, "A systematic method to obtain ultimate bounds for perturbed systems," *Int. J. Control*, vol. 80, no. 2, pp. 167–178, Feb. 2007.
[31] F. Stoican, S. Olaru, J. A. De Doná, and M. M. Seron, "Zonotopic ultimate bounds for linear systems with bounded disturbances," *IFAC Proc. Volumes*, vol. 44, no. 1, pp. 9224–9229, Jan. 2011.
[32] W. Yang, J. Gao, G. Feng, and T. Zhang, "An optimal approach to output-feedback robust model predictive control of LPV systems with disturbances," *Int. J. Robust Nonlinear Control*, vol. 26, no. 15, pp. 3253–3273, Oct. 2016.
[33] J. J. Martinez, N. Loukkas, and N. Meslem, "H-infinity set-membership observer design for discrete-time LPV systems," *Int. J. Control*, vol. 93, no. 10, pp. 2314–2325, Oct. 2020.
[34] J. Tan, H. Zheng, X. Wang, B. Liang, and W. Yang, "Computation of minimal detectable fault under hybrid stochastic and deterministic framework," in *Proc. Amer. Control Conf. (ACC)*, Jun. 2022, pp. 3620–3625.
[35] C. Combastel, "Zonotopes and Kalman observers: Gain optimality under distinct uncertainty paradigms and robust convergence," *Automatica*, vol. 55, no. 1, pp. 265–273, 2015.
[36] H. Pacejka, *Tire and Vehicle Dynamics*. Amsterdam, The Netherlands: Elsevier, 2005.
[37] H. B. Pacejka and E. Bakker, "The magic formula tyre model," *Vehicle Syst. Dyn.*, vol. 21, pp. 1–18, Jan. 1992.
[38] S. Ifqir, V. Puig, D. Ichalal, N. Ait-Oufroukh, and S. Mammar, "Zonotopic set-membership estimation for switched systems based on wi-radius minimization: Vehicle application," *IFAC-PapersOnLine*, vol. 53, no. 2, pp. 7446–7451, 2020.
[39] T. Alamo, J. M. Bravo, and E. F. Camacho, "Guaranteed state estimation by zonotopes," *Automatica*, vol. 41, no. 6, pp. 1035–1043, Jun. 2005.
[40] M. Pourasghar, V. Puig, and C. Ocampo-Martinez, "Robust zonotopic observer design: Interval observer versus set-membership approaches," in *Proc. 4th Conf. Control Fault Tolerant Syst. (SysTol)*, Sep. 2019, pp. 189–194.
[41] S. Zhang and V. Puig, "Robust fault detection using set-based approaches," in *Proc. 5th Int. Conf. Control Fault-Tolerant Syst. (SysTol)*, Sep. 2021, pp. 91–96.
[42] S. Zhang, V. Puig, and I. Sara, "Robust fault detection using set-based approaches for lpv systems: Application to autonomous vehicles," *IFAC-PapersOnLine*, vol. 55, no. 6, pp. 31–36, 2022.
[43] F. Xu, F. Stoican, V. Puig, C. Ocampo-Martinez, and S. Olaru, "On the relationship between interval observers and invariant sets in fault detection," in *Proc. Conf. Control Fault-Tolerant Syst. (SysTol)*, Oct. 2013, pp. 49–54.
[44] M. Althoff, "Reachability analysis and its application to the safety assessment of autonomous cars," Ph.D. dissertation, Dept. Elect. Eng., Technische Universität München, München Germany, 2010.

Shuang Zhang received the bachelor's and master's degrees from the Department of Control Engineering, Harbin Institute of Technology, Harbin, China, in 2018 and 2020, respectively. She is currently pursuing the Ph.D. degree in automatic control, robotics, and computer vision with Universitat Politècnica de Catalunya (UPC), Barcelona, Spain. Her research interests include fault diagnosis, fault tolerant control, robust control, set-membership, and linear parameter varying systems and switched systems.

Vicenç Puig received the B.Sc./M.Sc. degree in telecommunications engineering and the Ph.D. degree in automatic control, vision, and robotics from Universitat Politècnica de Catalunya–BarcelonaTech (UPC), in 1993 and 1999, respectively. He is currently a Full Professor with the Automatic Control Department, UPC, and a Researcher with the Institut de Robòtica i Informàtica Industrial (IRI), CSIC-UPC. He is the Director of the Automatic Control Department and the Head of the Research Group on Advanced Control Systems (SAC), UPC. He has developed important scientific contributions in the areas of fault diagnosis and fault tolerant control, using interval and linear-parameter-varying models using set-based approaches. He is also the Chair of the IFAC Safeprocess TC Committee 6.4. He was the General Chair of the 3rd IEEE Conference on Control and Fault-Tolerant Systems (SysTol 2016) and the IPC Chair of IFAC Safeprocess 2018.

Sara Ifqir received the master's degree in electronics, electrical energy, and automatic control (with a specialization in mobile autonomous systems) in 2016 and the Ph.D. degree in automatic control from the University of Paris-Saclay, France, in 2019. She is currently an Associate Professor with the Centrale Lille Institut, France. Her current research interests include nonlinear and switched systems, robust control, set-membership estimation, and fault diagnosis for complex physical systems, with a special focus on the fields of intelligent vehicles.